Performance Characterization of High-Density Electrospray Thrusters

Performance Characterization of High-Density Electrospray Thrusters

IEPC-2024-811

Presented at the 38th International Electric Propulsion Conference, Toulouse, France
June 23-28, 2024

Matthew N. Corrado*, Charity Wangari†, and Michael R. Finch‡
Massachusetts Institute of Technology, Cambridge, Massachusetts, 02139, USA

Lalitha Parameswaran, Matthew Cook, Eric C. Holihan, Richard Mathews, Jakub Kedzierski, Livia M. Racz, and Melissa A. Smith
MIT Lincoln Laboratory, Lexington, Massachusetts, 02421, USA

Paulo C. Lozano§
Massachusetts Institute of Technology, Cambridge, Massachusetts, 02139, USA

Research and development into electrospray propulsion technology has accelerated in recent decades. The state of the art in electrospray propulsion is microfabricated, passively-fed, ionic liquid electrospray thrusters operating in or near the pure ion regime. Passively-fed thrusters eliminate the need for complex and bulky flow regulation hardware and thus allow for the realization of one of the most attractive benefits of electrosprays, which is their ability to be scaled to extremely small sizes and masses. However, scaling down the size of a thruster comes with performance penalties for extensive properties such as thrust. To circumvent this penalty, it is desirable to increase the thrust density of electrospray thrusters so that they can provide acceptable performance in small packages. One method for increasing thrust density in electrospray thrusters is to increase the density with which individual ion emitters are packed in an array. Here, we describe and test a design for an electrospray propulsion system that is well-suited for densification. The microfabricated silicon emitters can be packed into arrays with pitch at least as small as 50 µm without loss of geometric feature quality, enabling potential increases in thrust density by a factor of 100 or more compared to the state of the art. We tested a prototype version of these thrusters with a 676-tip, 254-µm-pitch emitter array and a single emitter tip representative of the individual tips in the full array. The single tip produced current magnitudes of 100–200 nA at voltages on the order of 1 kV, while the full array produced 150–200 µA at similar voltage levels. Retarding potential analysis, time-of-flight mass spectrometry, and angle-resolved current measurements were used to compute properties of the beams of both the single emitter and the full array. From these beam diagnositcs we estimate propulsive performance metrics of the thruster at current setpoints ranging from 50 µA to 150 µA in both the positive and negative firing polarities with EMI-BF_4 propellant.

I. Introduction and Motivation

Ionic liquid electrospray propulsion is a highly efficient and scalable form of electric space propulsion. Benefiting from the high storage density of a pre-ionized propellant, low heat dissipation and energy losses, and an intrinsically modular form, ionic liquid ion thrusters (ILITs) are well-suited for many space propulsion

*Ph.D. Candidate, Department of Aeronautics and Astronautics, mcorrado@mit.edu
†Ph.D. Candidate, Department of Aeronautics and Astronautics, cwangari@mit.edu
‡Undergraduate Student, Department of Aeronautics and Astronautics, mrfinch@mit.edu
§M. Alemán-Velasco Professor, Department of Aeronautics and Astronautics, plozano@mit.edu.

DISTRIBUTION STATEMENT A. Approved for public release. Distribution is unlimited.
This material is based upon work supported by the Department of the Air Force under Air Force Contract No. FA8702-15-D-0001. Any opinions, findings, conclusions or recommendations expressed in this material are those of the author(s) and do not necessarily reflect the views of the Department of the Air Force.

applications, especially those in which high efficiency is desired at small length scales. ILITs lack in comparison to other forms of electric propulsion such as Hall effect thrusters (HETs) and gridded ion engines (GIEs) in their usefulness as primary propulsion for medium and large satellites. The reason for this drawback is not that ILITs cannot be scaled up; in fact, their scalability toward smaller or larger sizes without loss of performance or efficiency is unparalleled. Instead, ILITs perform behind HETs and GIEs in thrust density, or thrust produced per unit area, so scaling to performance levels of plasma thrusters requires scaling to sizes that, while theoretically possible, are prohibitive. For larger satellites to be able to take advantage of the benefits of ILITs, it is desired to improve the state of the art in electrospray propulsion to meet or exceed the thrust density required for mainstream use on all classes of satellites.

Because the current state of the art in electrospray propulsion does not approach the theoretical limitations, the challenge of improving thrust density is one of practicality and implementation. In other words, methods for fabricating, assembling, and operating high-density thrusters are likely possible but have yet to be proven. However, several research efforts currently focus on the development of high-density electrospray thrusters, much of them leveraging silicon microfabrication techniques to manufacture dense arrays of ion emitters. Examples include recent research from Yokohama National University [1–3] and Ienai Space [4–6], among others. In theory, denser packing of emitters should correlate directly with increased thrust density. Here, we provide an update on one program targeting high-density electrospray propulsion, a collaboration between the MIT Space Propulsion Laboratory (MIT SPL) and MIT Lincoln Laboratory (MITLL).

While earlier versions of these high-density thrusters have been described and tested previously [7–9], initial results highlighted preliminary proof-of-concept testing and performance data. Here, we measure more wholly the parameters and performance metrics relevant in spacecraft design and over a wide range of operational conditions. Above merely demonstrating stable and reliable operation, we thoroughly characterize the performance of these high-density thrusters through several common diagnostic techniques, including current-voltage characterization (IV), retarding potential analysis (RPA), time-of-flight mass spectrometry (TOF), and angular current distribution. These measurements are combined to estimate relevant performance metrics of the thrusters at several operating points of interest. Relevant performance metrics include but are not limited to thrust (F), specific impulse (I_{sp}), and thrust efficiency (η_T). Another relevant performance characteristic, lifetime, is tested via a long-duration firing of a prototype thruster.

In addition to a full thruster array, characterization of a single emitter tip fabricated to be geometrically representative of any individual tip in an array was performed. Testing performed on the single tip was aimed to mirror the testing performed on the thruster array, but with the analysis focused on understanding and extrapolating the behavior of the full arrays rather than estimating propulsive performance. The single emitter results establish a baseline to which the array results can be compared. The arrays underwent a similar battery of tests, with additional emphasis on using the diagnostic results to infer thruster performance metrics. Fabrication of thruster components was performed at MITLL, while all testing was performed at MIT SPL.

II. Device Description

The basic architecture and technology involved in the high-density thrusters characterized in this work were described in detail in 2022 [9]. The emitters are fabricated from silicon wafers and are defined using a grayscale lithography process [10] followed by plasma etching to form cone-like emitter tips with smooth contours and small radii of curvature. A microcapillary array is etched through the substrate via deep reactive ion etching (DRIE) to form long, narrow capillaries through which propellant can flow uniformly from the backside of the emitter to the tip array. The silicon surface is texturized using a chemical etching process to encourage passive propellant transport along the surface of the array and tips due to capillary action in the thin porous surface layer that results.

The emitters can be fabricated into arrays of a wide range of densities. The development process of this thruster design has involved testing of different emitter versions, with the primary characterizing feature of any version being the emitter pitch and therefore the density with which the emitters are packed. Table 1 describes the various densities of emitters that have been fabricated, ranging from relatively low-density comparable to current state-of-the-art electrosprays with $\sim$500 µm spacing between emitters, to ultra-high-density emitters with pitch nearly a factor of 10 smaller than the state of the art. A factor of 10 decrease in pitch represents a factor of 100 increase in number of tips and theoretical thrust density, all else being equal. The arrays are arranged into uniform square grids of tips, the outer dimension of which is approximately

The 38th International Electric Propulsion Conference, P. Baudis Convention Center, Toulouse, France, June 23-28, 2024

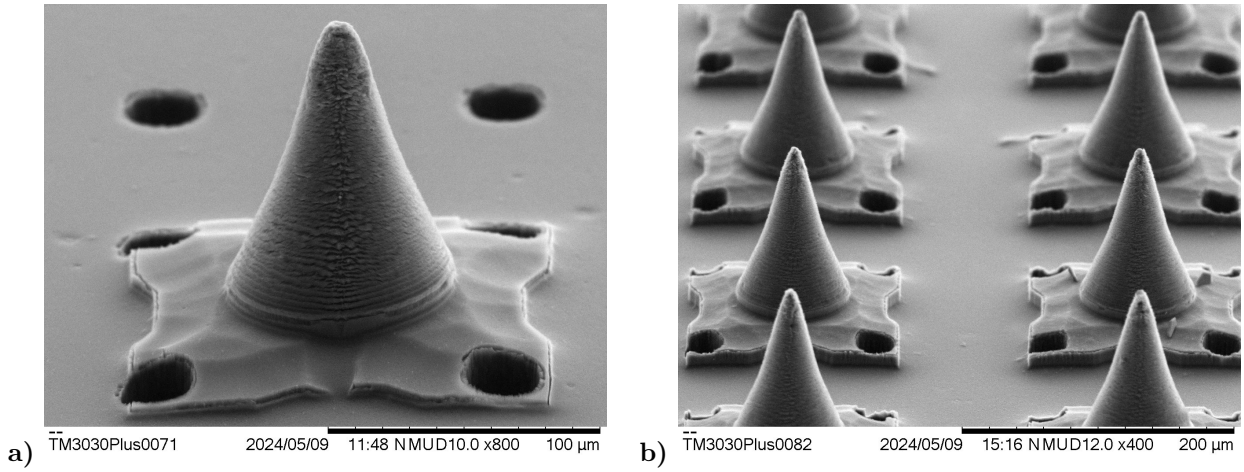

Figure 1. SEM micrographs of the devices tested here. (a) The single-tip emitter. (b) A section of the full emitter array.

6.6 mm for all density versions of the emitters. SEM micrographs of the single-tip emitter and the full emitter array tested in this work are provided in Fig. 1.

The extractor electrodes are also microfabricated in silicon using standard photolithographic and plasma etching processes. The thickness of the extractor grid is nominally ∼50 µm, and the aperture radius varies with emitter density, per Table 1. The extractors are coated with a layer of platinum to assist with making an electrical connection, which is typically done by soldering a wire to the structural rim of the chip. The emitter and extractor electrodes are separated by ceramic spacers positioned in all four corners of the chips, with the spacer thickness being approximately equal to the height of the tips, ∼100–200 µm depending on the version. Thruster chip stacks are typically aligned under a microscope to within 5–10 µm accuracy and bonded in place using a low-outgassing, electrically insulating epoxy.

Table 1. Various density levels of fabricated emitters and high-level geometric description. The rightmost column represents the number of tips inside a 6.6 mm by 6.6 mm square array.

Density	Emitter Pitch	Aperture Diameter	Number Tips
Low	508 µm	300 µm	169
Medium	254 µm	200 µm	676
High	127 µm	100 µm	2,704
Ultra-High	64 µm	50 µm	>10,000

III. Experimental Setup

The primary experimental test unit for this work was a medium-density thruster as defined in Table 1, i.e. a 676-tip, 254-µm-pitch array of grayscale-etched silicon emitter tips. The extractor electrode, consisting of a grid of 200-µm-diameter by 50-µm-thick apertures, was aligned and bonded to the emitter via electrically insulating spacers such that the apices of the tips were in the plane of the bottom surface of the extractor. Completing the thruster head was an additional silicon chip bonded below the emitter to serve as a physical interface with the propellant tank. The medium-density version of the emitters was chosen for baseline characterization because it represents an increase in density compared to the state of the art in flight-proven electrosprays but is not expected to exceed the level at which the factors that may limit densification, including but not limited to hydraulic limitations or space charge effects, become significant. It is not known precisely when or if thrust density is limited by these or other factors, but there is precedent for operating experimental electrospray thrusters with densities similar to that of the medium-density emitter tested here without issue. Thruster densities up to the high-density version have been successfully tested with integrated gridded extractors[9], and all versions including the ultra-high-density emitters have been tested against solid

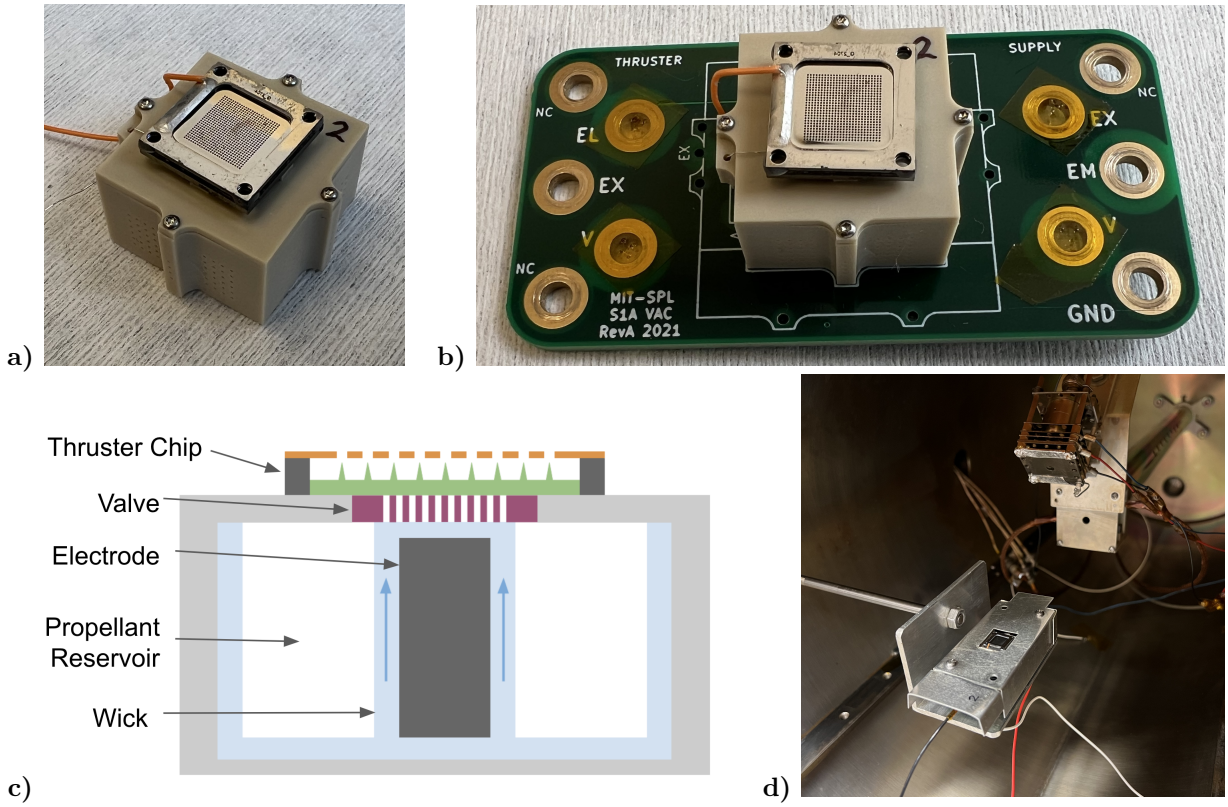

Figure 2. The thruster assembly characterized in these experiments. a) Angled view of the thruster mounted to the tank. b) The full thruster and tank assembly mounted to a custom electronics board for power and signals routing. (c) A cross-sectional diagram of the propellant tank. (d) An image of the thruster assembly mounted on a rotational stage in front of the diagnostic instruments inside the vacuum chamber.

extraction electrodes. More detailed performance data for all density levels will be the subject of future work.

The propellant tanks used for this characterization were nearly identical to those described by Petterson[11]. The tank design consists of a propellant reservoir with porous polytetrafluoroethylene (PTFE) walls and a cylindrical porous carbon xerogel electrode running through its center. A polyether ether ketone (PEEK) outer shell gives the reservoir structural support and provides physical interfaces. A PEEK cap seals the reservoir and serves as the interface between the reservoir and the thruster. The cap contains a slot for a single-use solid-state electrowetting valve, which prevents propellant from migrating from the reservoir to the thruster before it is actuated once the system is under vacuum and all materials and propellants have been allowed time to outgas. The design, operating principle, and testing of the electrowetting valves have been described in detail in previous works[12–14]. A network of paper and glass fiber wicks establish fluidic continuity between and through the reservoir, electrode, valve, and thruster. Different from the previous works cited above, the reservoirs used in these tests were filled with a porous polyvinyl alcohol (PVA) foam with approximately 90% porosity and a mean pore diameter of approximately 100 µm. The negative pressure afforded by the porous reservoir controls the wetting state at the emitter surface once the valve is actuated and the emitter is wetted in vacuum.

The full thruster and tank assembly was mounted to a custom electronics board designed to interface both physically and electrically with the propellant tank, shown in Fig. 2(b). The board provides electrical breakouts for the emitter, extractor, and valve electrodes so that they can be connected through vacuum feedthroughs to laboratory power supplies and equipment. A grounded aluminum shield with a cutout for the thruster head was placed over the electronics board to electrically shield the high-voltage electronics and sensitive current signals from the thruster and to maintain zero potential in the plane of the extractor electrode in the immediate vicinity of the thruster. The propellant used for all tests performed in this work was 1-ethyl-3-methylimidazolium tetrafluoroborate (EMI-BF_4).

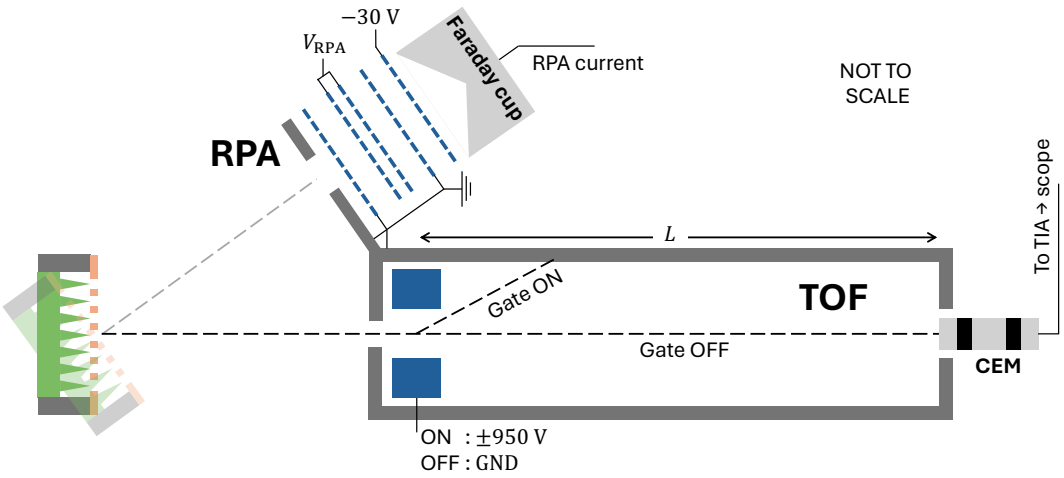

Figure 3. Diagram of the diagnostic layout in the vacuum chamber.

The thruster head for the single-tip emitter was identical to the full thruster array in all ways except for the number of tips. The single-tip emitter was fabricated using the same process as the arrays but was masked during the photolithography in such a way to produce only one tip in the center of the chip. All other aspects of the emitter and extractor were identical, including the diameter and thickness of the extractor aperture. Rather than being mounted to the same type of tank as the full thruster, the single emitter was fixed to a smaller custom mount machined from PEEK. However, propellant storage and transport in and through the custom mount were designed to be nearly identical to that in the full tank, only on a smaller scale to minimize propellant and consumable hardware waste. Therefore, the single emitter mount used a PVA foam reservoir, a network of paper and glass wicks, and a porous carbon electrode.

During operation, the extractor electrodes were grounded and the electric potential on the emitters was controlled using a Matsusada AP-3B1 high-voltage amplifier with a range of −3 kV to 3 kV and capable of sourcing up to 1 mA of current. Current through the emitter and extractor were monitored independently using shunt resistors with Analog Devices AD210AN isolation amplifiers. The integrated thruster assembly was tested in the Turbovac vacuum facility in the MIT SPL. The Turbovac chamber is pumped by two turbomolecular pumps totaling 750 L/s pumping capacity and backed by a dry roughing pump. Chamber pressure was maintained below 5×10^{-6} Torr during all portions of the tests. The thruster, tank, and electronics board assembly were mounted on a rotational stage with an angular encoder so that the thruster could be pointed toward different diagnostic instruments positioned along an arc approximately 10 cm from the thruster face, as shown in Fig. 2(d).

The primary diagnostic instruments used to measure properties of the ion beams and estimate performance were a time-of-flight mass spectrometer (TOF) and a retarding potential analyzer (RPA). The layout of the instruments is diagrammed in Fig. 3. The TOF consists of an electrostatic deflection gate and a current collector separated by a long grounded tube. An ion beam enters into the tube through a 5 mm aperture before passing through the gate. When the gate is on, +950 V and -950 V are applied to the two gate electrodes, respectively, generating a strong electric field normal to the ion trajectory which deflects the beam to be absorbed by the grounded tube prior to reaching the current collector. When the gate is off, the gate electrodes are grounded so that the ion beam passed through the gate and toward the current collector unperturbed. After some flight time that depends on the flight length separating the gate and the collector, L, and the velocity of the ions, c, the ions are registered by the collector.

The current collector used in the TOF instrument is a Photonis MAGNUM 5900 channel electron multiplier (CEM). The gain of the CEM, exceeding 10^7, enables efficient time-resolved detection of extremely low ion currents resulting from sampling a small, axially-directed portion of the beam to minimize signal noise due to flight length differences. The CEM signal is fed to a custom transimpedance amplifier (TIA) and routed to an oscilloscope for interpretation and recording. The gate is controlled by a square wave from a signal generator fed through a high-voltage pulse amplifier. The gate cycling frequency for these experiments was set to 100 Hz.

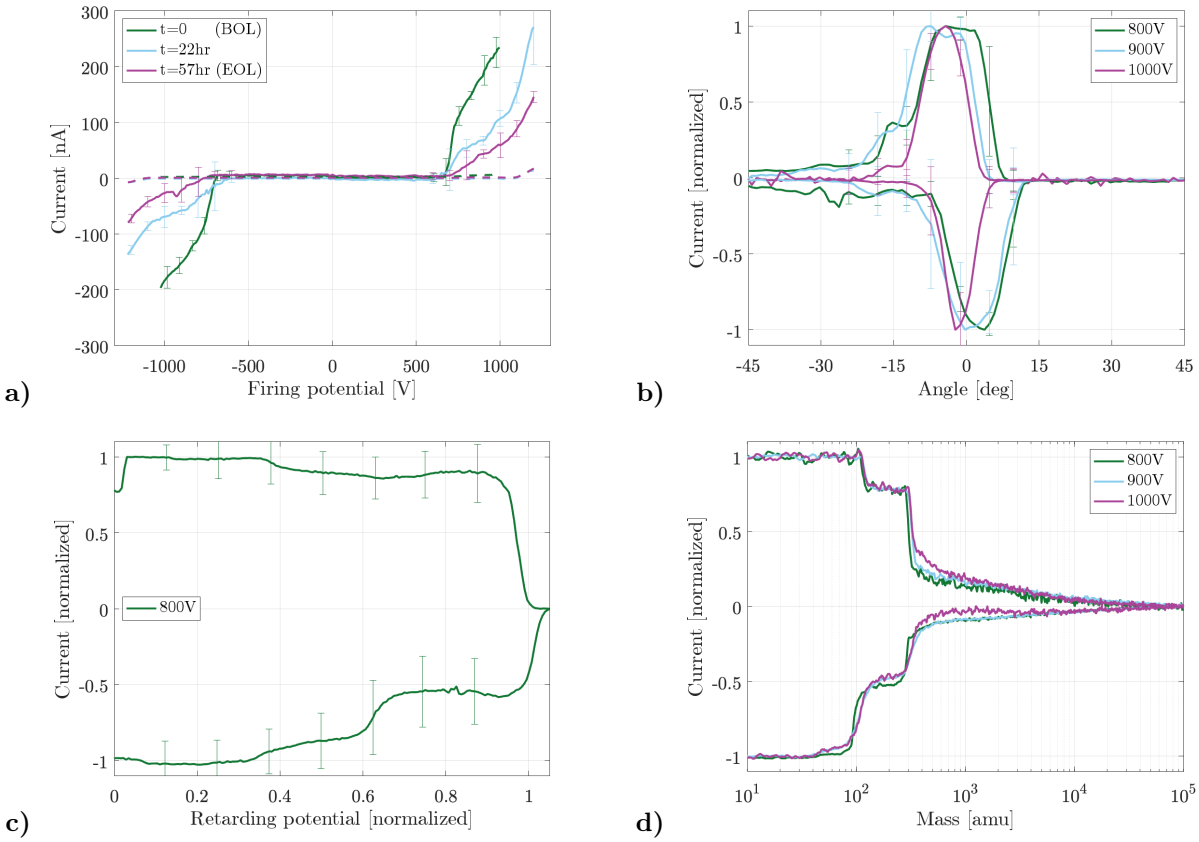

Figure 4. Diagnostic data collected for the single-tip emitter at different voltage setpoints. Error bars represent the 3σ uncertainty. (a) IV. (b) Angular. (c) RPA ($\pm$800 V only). (d) TOF.

The RPA instrument consists of an aperture for sampling a narrow section of the beam, followed by a series of isolated high-transparency grids, behind which sits a Faraday cup to register the ion current that passes through all the grids. As illustrated in Fig. 3, a series of variably-biased stopping grids are shielded on either side by grounded grids, and an electron-repelling grid biased to -30 V is positioned immediately upstream of the Faraday cup to keep low-energy secondary species from interfering with the current signal. The RPA hardware is used for multiple measurement types. First and most obviously, the bias on the stopping grids, V_{RPA}, can be swept between zero and the emitter potential to sample the energy spectrum of the ion beam. In addition, with the stopping grids grounded the instrument is used as a simple Faraday probe to measure the angular current distribution of the ion beam. For angular measurements, the relative angle between the thruster and RPA centerlines is swept between $-90°$ and $+90°$.

IV. Single Emitter Results

Following a brief conditioning period to ensure that the emitter had reached steady state, diagnostic data were collected from the single emitter over the course of several hours during which TOF, RPA, and angular measurements were taken at various applied voltages. Electrosprays are typically operated in a current-controlled manner because thrust is tied most strongly to current. However, the single emitter was controlled by voltage because it is difficult to know the magnitude of current being emitted from any individual emitter in an array, and in fact it has been observed that the currents emitted by tips across an equipotential array can exhibit a large degree of nonuniformity [15]. Therefore, it may not be sufficient to divide a target array current by the number of tips to determine a target tip current. However, the voltage applied to each tip in an array is always known and uniform, so diagnostic data as a function of voltage may be most illuminating, especially if the voltages represent those required to achieve the target currents for an array. In our case, the single emitter started emitting at just above 700 V, so data were collected with the tip

firing at ±800 V, ±900 V, and ±1000 V to cover the expected range of full array operating conditions. After all measurements were taken, the tip was set to fire continuously to failure. During this continuous firing period, voltage magnitude was held constant (but manually adjusted periodically) and voltage polarity was alternated with a period of 10 s.

After approximately 4 hours of probe data collection, the emitter fired in the continuous mode for more than 50 hours. At the time that the test was terminated, the emitter was still operating, but the current had depleted and become unstable, so the test was voluntarily ended. In addition to the TOF, RPA, and angular measurements, IV curves were recorded for the emitter at various times during the testing period. Beginning-of-life (BOL) and end-of-life (EOL) IV curves were taken in addition to one taken in the middle of the continuous firing period.

All three IV curves are plotted in Fig. 4(a). It can be seen that the behavior of the emitter changed over time. At BOL the IV behavior was close to ideal, with a large jump in current at the onset voltage followed by a linear rise in current with voltage. As the test progressed, not only did the emitter continue to deviate from this near-ideal behavior but also the slope of the IV curve decreased noticeably. In other words, the tip emitted much less current at the same voltage at EOL compared to BOL. A decrease in IV slope can, in general, be the result of an increase in fluidic resistance, so it is possible that the emitter began to experience a hydraulic limitation or became starved of propellant. The reservoir feeding the tip was filled with 50 µL of EMI-BF_4, which would ideally be capable of sustaining emission on the order of 100 nA with an average charge-to-mass ratio (q/m) of 100 C/g for upwards of 10,000 hours. However, the propellant storage and feeding setup was far from optimized and the foam reservoirs used for these tests were experimental and their properties were not perfectly known. As such, it is possible that the volumetric fill fraction in the foam reached a level that could correspond to a large increase in negative pressure above that which was anticipated, therefore slowing propellant flow. It was also considered that the emitter could have experienced some physical or chemical degradation which either altered the geometry of the tip or altered the properties of the fluid path feeding emission, increasing hydraulic impedance. However, detailed imaging of the emitter after the test showed no evidence of degradation.

Angular scans of the emission across a single rotational axis are given in Fig. 4(b). The beams are rather narrow, with half-angles encompassing 90% of the beam on the order of 10–15° at all operating points. Also noticeable about the angular measurements are the offset in the central firing angle between the positive and negative modes, indicating that the emitting meniscus changes in shape, location, or both between the two modes. This offset is approximately 5–10°. The width of the angular distributions are also fairly consistent with voltage, with the only trend being a slight narrowing of the beam with voltage.

Due to constraints with the diagnostic instruments, RPA data for the single emitter were taken at only the 800 V condition. The RPA curves in Fig. 4(c) show evidence of fragmentation in the field-free region occurring in both polarities, though to different extents. In the positive mode, the most significant step in current is seen at an energy fraction of 0.36, corresponding to dimer-to-monomer fragmentation events. In the negative mode, a small step is seen at the dimer-to-monomer energy fraction of 0.30, but it is overshadowed by a much larger step at 0.59, which is the energy fraction corresponding to trimer-to-dimer fragmentation events.

The TOF measurements recorded at all 3 conditions in both polarities are given in Fig. 4(d). The TOF results reveal a slightly smaller fraction of monomers and a slightly larger fraction of heavy species (i.e. heavier than trimers) in the positive mode as compared to the negative mode. The negative mode curves show a roughly even split between monomers and dimers with very few heavy species. In both polarities, the TOF traces are fairly consistent across the different operating conditions. More discussion on the meaning and implications of individual diagnostic measurements will be included in the next section.

V. Thruster Array Results

The full thruster array fired for a total of approximately 10.5 hours, the first 4.5 of which consisted of diagnostic measurements at 3 prescribed current setpoints in both firing polarities, while the final 6 hours were continuous firing at constant voltage with polarity alternation. The test was terminated when a permanent short circuit developed between the emitter and extractor electrodes, characterized by a sudden increase in current through both electrodes to the point of saturation of the current sensing circuitry.

The three operating setpoints chosen for the characterization were ±50 µA, ±100 µA, and ±150 µA. These were selected based on assumed performance of this version of the thrusters resulting from previous

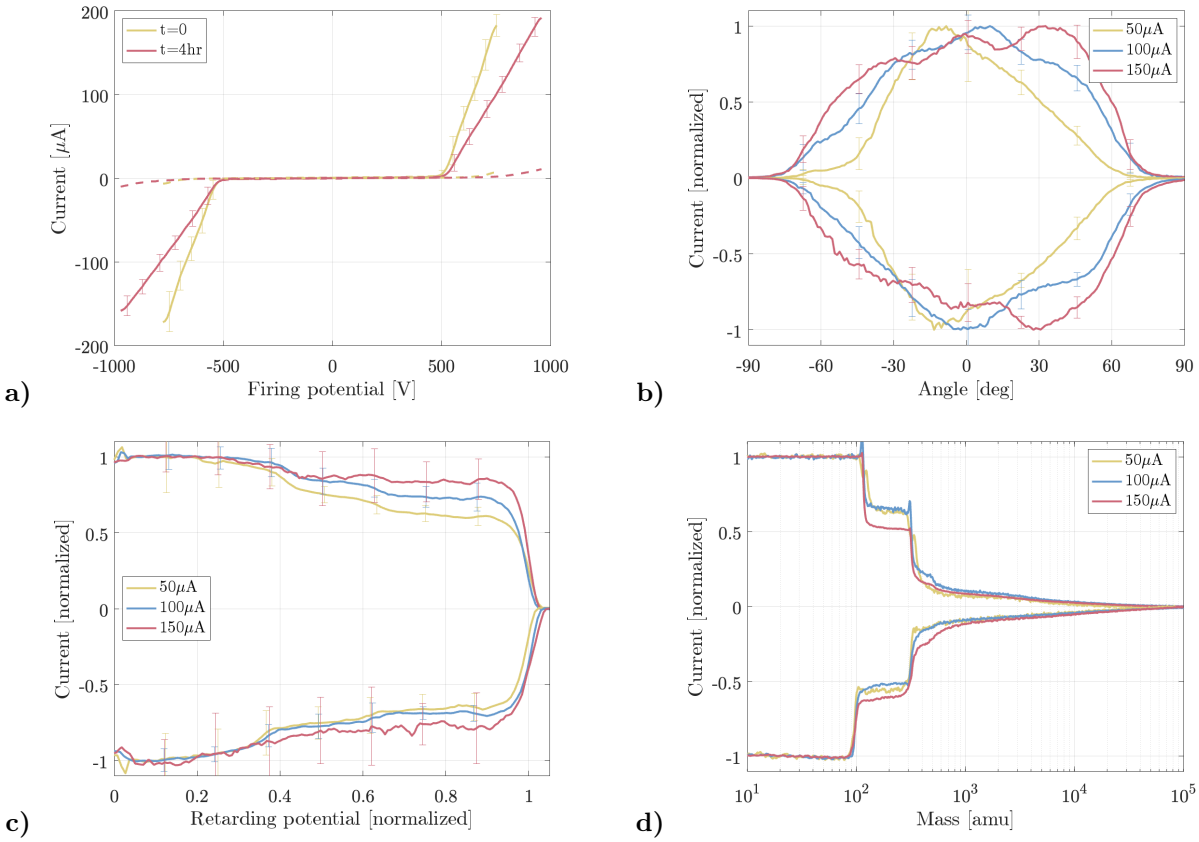

Figure 5. Diagnostic data collected for the full array thruster at different current setpoints. Error bars represent the 3σ uncertainty. (a) IV. (b) Angular. (c) RPA. (d) TOF.

preliminary testing. Figure 5(a) shows current-voltage (IV) curves recorded before and after the primary diagnostic measurements were acquired. These traces show that the thruster was capable of reaching all three target setpoints throughout the diagnostic period, and at reasonable voltages and relatively low levels of intercepted current. However, it is noteworthy that the IV curves show a change in behavior of the thruster over the 4.5-hour diagnostic period. In particular, while the startup potential and interception rate remained constant, the slope of the IV curve underwent a dramatic change, becoming much shallower from hour 0 to hour 4 beyond the uncertainty of the measurements. Possible causes for this change in behavior and any implications that it may have on the performance estimates will be discussed in more detail below.

During the 4.5-hour diagnostic period, the thruster was operated at a constant voltage in one polarity at a time. First, the positive and negative voltages that produced the desired current level were found, at which point raw TOF data were acquired in each polarity followed by raw angular and RPA data, in that order. Measurements were repeated for each diagnostic type in both polarities at least three times so that the resulting data could be averaged during post processing. Once all measurements were completed in both polarities at a given current setpoint, the procedure was repeated for each of the other current levels.

Figure 5(b)-(d) show plots of averaged angular, RPA, and TOF measurements, respectively. For the angular and RPA data, current is normalized by the maximum average collector current for each setpoint. For the TOF data, current is normalized between the mean signal level prior to the first detectable current step and the mean signal level after the point at which the current reaches a constant value. For all measurement types, curves were averaged by grouping the independent variable (emitter potential, angle, retarding potential, or mass for IV, angular, RPA, and TOF measurements respectively) into bins of fixed width and averaging the value of the dependent variable (usually emitted or collected current) inside those bins. The bin widths used in processing the data displayed in Fig. 5 were 10 V, 1°, and 5 V for the IV, angular, and RPA data respectively. The TOF data were binned on a logarithmic scale to increase the sampling density in the most interesting range of masses.

Figure 5(b) illustrates how the angle that envelopes a given fraction of the beam increases with beam current, a result seen in previous work with porous electrospray emitter arrays and EMI-BF_4 propellant [16]. The increased spreading of the beam with current is dissimilar to what is seen for the single emitter for which the beam either remains constant or becomes more narrow with voltage. The likely explanation for this is that each of the hundreds of tips in the array fire in slightly different directions, so the overall beam angle is much larger than that for any individual beamlet. The array beams may continue to increase in spread with current due to the activation of deformed tips or activation of secondary emission sites at the higher voltages, these secondary beams more likely to be firing off-axis. This angular spread of beam current impacts the performance of the thruster through the angular efficiency, for which we use the definition suggested by Ziemer [17], $\eta_\theta = (F_{real}/F_{ideal})^2$. This ratio can be expressed in terms of measured quantities using Eq. 1, according to Petro [18]. The central angle, θ_c, of the beam is defined as the angle at which the current integrals to the left and to the right of θ_c are equal, which amounts to solving Eq. 2 numerically.

$$\eta_\theta = \left(\frac{\int_{\theta_c - \frac{\pi}{2}}^{\theta_c + \frac{\pi}{2}} I(\theta) \cos\theta \sin\theta d\theta}{\int_{\theta_c - \frac{\pi}{2}}^{\theta_c + \frac{\pi}{2}} I(\theta) \sin\theta d\theta} \right)^2 \tag{1}$$

$$\int_{-\frac{\pi}{2}}^{\theta_c} I(\theta) d\theta \equiv \int_{\theta_c}^{\frac{\pi}{2}} I(\theta) d\theta \tag{2}$$

Noteworthy regarding the angular distributions is not only the observation that they become more spread with increased current but also their tendency to become increasingly asymmetric and multimodal, trends that are consistent in both firing polarities. We did not find evidence that these latter effects are universal among ionic liquid electrospray thrusters, and so it is possible that the cause for this is in a peculiarity unique to the thrusters tested here. One plausible explanation is that defects on the emitter tips enable activation of new, off-axis emission sites at the higher firing voltages. This hypothesis could be tested in part by probing the spatial distribution of current across the thruster face with sufficiently high resolution to determine the status of individual emitter tips, similar to the experiments performed by Guerra-Garcia [15].

The RPA curves in Fig. 5(c) yield insight into the energy spectra of the ion beams as a function of current. The curves show evidence of significant amounts of fragmentation events transpiring in the field-free region, i.e. outside of the thruster. Field-free fragmentation events yield child ions with energies equal exactly to the mass fraction of the child relative to its parent. For EMI-BF_4, the most relevant mass fractions in the positive mode are 0.22, 0.36, and 0.61 for fragmentation of trimers into monomers, dimers into monomers, and trimers into dimers, respectively. In the negative mode, the analogous fractions are 0.18, 0.30, and 0.59. Our RPA measurements show evidence of all these event types in the range of currents tested.

Some trends in the RPA measurements exist that are common among all the current setpoints and both polarities. For instance, it is clear that the most prevalent fragmentation event at all conditions is the dimer-to-monomer event, as evidenced by the height of the current steps at energy fractions of 0.36 in the positive mode and 0.30 in the negative mode. For all conditions, smaller current steps exist at the energy fractions corresponding to trimer-to-dimer events, and only at some of the conditions is there a clear step at the expected location of trimer-to-monomer events. Noticeably absent from the full array RPA scans is the large trimer-to-dimer step in the negative mode that was seen in single emitter measurements. In addition to these trends, it is evident that in both polarities the relative abundance of field-free fragmentation events decreases with current. For example in the positive mode, we see that at 50 µA approximately 40% of the ions have energies less than the beam energy at the time they reach the RPA instrument, while at 150 µA this fraction decreases to about 20%. This trend is less significant in the negative mode. It is worth noting that it appears that most of these lower-energy ions are the result of field-free fragmentation, which does not have a significant negative impact on performance in most cases. As expected, the largest and most prominent current step in all RPA measurements is near the applied firing potential, indicating that there are minimal energy losses in the emission and extraction process. To evaluate this quantitatively, we define energy efficiency as the ratio of the actual beam potential to the applied emitter potential, and we take the beam potential to be the retarding potential at which the largest change in collected current is observed, Eq. 3.

$$\eta_E = V_{RPA} \left(\max \left| \frac{dI_{RPA}}{dV_{RPA}} \right| \right) \Big/ V_{em} \tag{3}$$

TOF measurements yield some of the most practical performance estimates for space propulsion purposes. The directly-measured spectrum of charged particle velocities can be converted, through simple but reasonable assumptions, to a spectrum of ion masses and charge-to-mass ratios. The data in Fig. 5(d) are shown as a function of particle mass using the assumption that ions reaching the TOF detector are singly-charged. For EMI-BF_4, the most relevant masses in the positive mode are 111 amu, 309 amu, and 507 amu for monomers, dimers, and trimers, respectively. In the negative mode, the analogous masses are 87 amu, 285 amu and 483 amu. Our measurements reveal a fairly constant beam composition as a function of current in the range tested, at least qualitatively. Most of the measurements showed approximately 45% each of monomers and dimers, a small percentage of trimers, and approximately 10% of heavier species. However, these rough percentages do not exactly describe all of the measurements, and small deviations of each measurement from these rough averages can yield significant differences in calculated performance estimates. It can be noted that the TOF measurements for the full array align well with those for the single emitter in that most of the positive-mode scans exhibit a smaller fraction of monomers and a larger fraction of heavy species, as compared to the negative-mode scans. The differences are not as pronounced as they appeared for the single emitter, which is likely due to the superposition of the hundreds of ion beams in the full array, each of which may be behaving slightly differently, creating an averaging effect.

Equations 4 and 5 are used to estimate thrust and mass flow rate, respectively, based on TOF measurements where V is the firing potential, L is the flight length, I_{tot} is the total emitted current at the time of the measurement, and $\bar{I}(t)$ is the TOF detector current as a function of time after gate opening, normalized between 0 and 1 as described previously. The weighted average exhaust velocity is calculated as $c = F_{TOF}/\dot{m}_{TOF}$, and specific impulse is $I_{sp} = c/g_0$ where g_0 is Earth's gravitational constant.

$$F_{TOF} = \frac{2V}{L} I_{tot} \int_0^\infty \bar{I}(t) dt \tag{4}$$

$$\dot{m}_{TOF} = \frac{4V}{L^2} I_{tot} \int_0^\infty \bar{I}(t) t dt \tag{5}$$

It is important to note that metrics like thrust, specific impulse, and mass flow rate inferred from TOF are merely estimates of the true performance. There is a wealth of literature that describes the limitations of TOF-based performance estimates, but they are generally acceptable for order-of-magnitude approximations or better and are capable of capturing trends. TOF-based thrust in particular will almost always overestimate true thrust without proper adjustments. This is because F_{TOF} does not account for angular beam spread or interception, among other loss mechanisms. It has been shown that correcting F_{TOF} for angular efficiency yields estimates that are comparable to "true" thrust measured through direct methods[16,19,20], as angular efficiency is typically one of the largest thrust reduction mechanisms not captured by TOF.

One loss mechanism that can be captured, at least to some extent, by TOF measurements is polydispersive efficiency, η_p. Polydispersive efficiency can be estimated by considering the thrust power, $F^2/2\dot{m}$, calculated from the TOF estimates and comparing it to the electric power input, VI. This essentially represents the minimum power loss experienced by the thruster due only to the presence of species with different q/m being accelerated through the electric field, and it is given by Eq. 6.

$$\eta_p = \frac{F_{TOF}^2/2\dot{m}_{TOF}}{V I_{tot}} \tag{6}$$

The final measurable and potentially-significant loss mechanism not yet explicitly discussed is the transmission efficiency, η_{tr}, which accounts for the fraction of the beam that is intercepted by the extractor electrode and therefore does not contribute to thrust. Because current through the emitter and through the extractor, I_{em} and I_{ex}, were measured independently throughout testing, η_{tr} can be calculated simply as the ratio of the unintercepted current, $I_{em} - I_{ex}$, to the total current through the emitter. This was done by averaging both current measurements over all intervals during which the thruster was firing at a given current setpoint. Relative intercepted current grew slightly at the higher current setpoints compared to the lower ones, which is a common observation for porous or rough externally-wetted electrospray thrusters due to the tendency for secondary emission sites to activate at higher voltages, these secondary emission sites typically firing off-axis. Notwithstanding, intercepted current was relatively low at all operating points, yielding large values of η_{tr} between 0.95 and 0.99.

A summary of all estimated performance metrics calculated from diagnostic measurements as described above is given in Table 2. Power, P, represents the power through the thruster only and is calculated as

Table 2. Summary of performance estimates from IV, TOF, RPA, and angular probe measurements. TOF-based estimates are corrected for angular and transmission efficiencies.

I_{em} [µA]	I_{ex} [µA]	V [V]	P [mW]	F_{TOF} [µN]	$I_{sp,TOF}$ [s]	$\dot{m}_{TOF}$ [µg/s]	η_p	η_θ	η_{tr}	η_E	η_T
50	0.8	610	31.7	2.8	808	0.35	0.58	0.68	0.98	0.98	0.37
100	1.8	714	70.3	6.2	574	1.10	0.47	0.57	0.98	0.99	0.25
150	6.0	843	127.2	9.1	587	1.58	0.42	0.53	0.96	0.99	0.21
-50	-0.7	-622	31.8	3.1	425	0.60	0.39	0.68	0.99	>0.99	0.25
-100	-2.7	-731	72.1	5.8	509	1.17	0.38	0.56	0.97	>0.99	0.20
-150	-7.9	-890	132.4	10.6	451	2.39	0.37	0.52	0.95	>0.99	0.18

$P = VI_{em}$. The TOF-based thrust and specific impulse estimates reported in Table 2 are corrected for angular and transmission efficiencies by applying a multiplicative factor of $\eta_{tr}\sqrt{\eta_\theta}$ to the raw calculations in order to account for real thrust loss due to beam spreading and interception. An energy correction was omitted because $\eta_E \approx 1$ for all cases. The total efficiency, η_T, represents the ratio of the *actual* thrust power (corrected for all measured losses) to the input electric power, and is therefore calculated using Eq. 7.

$$\eta_T = \eta_{tr}^2 \eta_\theta \eta_E \eta_p. \tag{7}$$

Note that additional loss mechanisms may exist in electrospray thrusters, but the ones discussed and estimated here are hypothesized to be the most significant ones.

After completing the primary data-collection phase of the experiments, the thruster was fired continuously to propellant depletion or to failure, whichever occurred first. The emitter potential was set to a voltage of constant magnitude and alternating polarity, with the period of alternation being 10 s. The voltage was initially set to ±800 V to target a constant current of approximately ±100 µA. However, the thruster's current output decayed at a near-constant rate in both polarities to ∼75 µA over the span of about 1.5 hours, at which point the voltage magnitude was increased to 850 V. The current continued to decay, and after another 4.5 hours the current had reached ∼50 µA and the test was concluded after a short circuit developed between the emitter and extractor electrodes. The current emission behavior over this 6-hour continuous firing period is shown in Fig. 6. This long-term current decay is similar to the trends observed for the single emitter between BOL and EOL and to the thrends in the IV curves measured for the full array before and after the diagnostics phase. Much like with the single emitter test it is unlikely that the propellant in the tank was depleted, and direct mass loss measurements confirm that $< 5\%$ of the original propellant mass was consumed. Instead, the behavior of both test articles suggests that there is some still-unknown factor contributing to the current decay. It is merely speculative to assume the root cause, but possibilities include chemical or physical degradation of the emitter as surmised earlier or a growing bottleneck somewhere in the fluidic network that worsens over time.

The mass of the thruster assembly was measured using a precision mass balance immediately before and after testing to determine propellant consumption. All thruster materials, including the propellant itself, were outgassed in vacuum prior to these measurements to prevent mass loss due to outgassing from corrupting the propellant consumption measurement. The direct measurement using the precision balance yielded a mass loss of (58.5 ± 1.9) mg. The uncertainty in this measurement comes from the precision of the mass balance and from averaging repeated measurements. We can compare this to an indirect estimate for propellant consumption computed from the current emission data and TOF measurements. To compute the indirect mass loss, all thruster data, including those during the conditioning and diagnostic phases, were combined. Instantaneous mass flow rate was estimated by interpolating the TOF-derived values for $\dot{m}$ from Table 2. This $\dot{m}(t)$ was integrated over all firing periods to compute a total Δm, which came to (28.1 ± 5.7) mg. The uncertainty in this calculation is derived from the uncertainty in the TOF curves themselves. The difference between the direct and indirect estimates of propellant consumption suggests a mass utilization efficiency of approximately 48%, with the remaining 52% of mass being unaccounted for. Explanations for this phenomenon are beyond the scope of this work but may include electrochemical reactions, neutral propellant evaporation, or an underestimation of the uncertainty of the TOF measurements, among others.

By integrating just the emitted current over time, we can calculate that a total of 1.375 C and 1.185 C of positive and negative charge were emitted, respectively. Using the directly-measured propellant consumption,

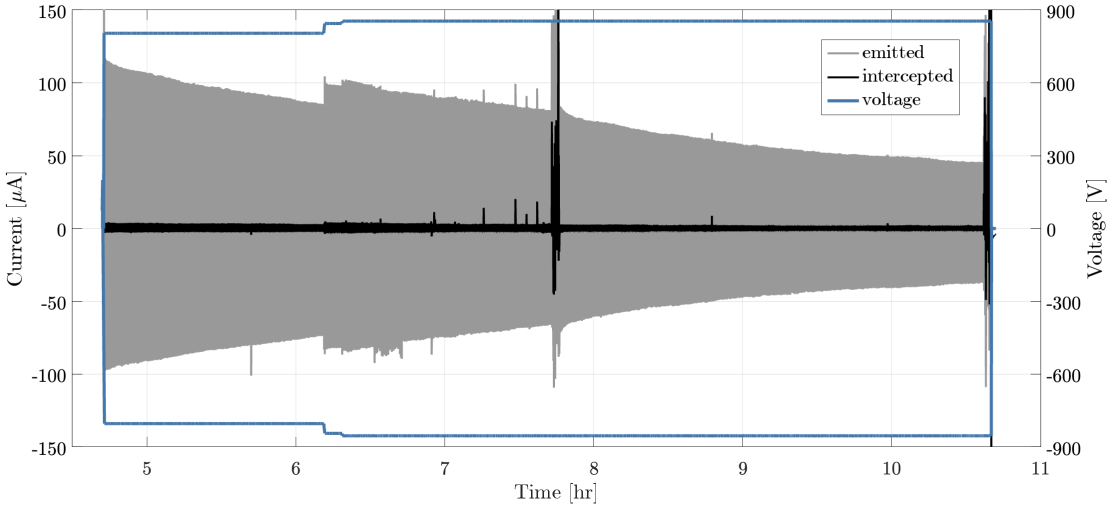

Figure 6. Constant-voltage lifetime test, cut short after approximately 6 hours of continuous bipolar firing due to a short circuit.

this yields an average q/m of 43.8 C/g. Taking the average voltage magnitude over the continuous firing period, 836 V, as an indicator for the timed-averaged voltage over all firing periods, we calculate an estimate for the average ideal specific impulse of 872 s. Note that this $I_{sp,ideal}$ represents the case in which specific impulse is calculated from actual mass consumption and emitted current, and it does not rely on TOF. The I_{sp} estimates from TOF alone, listed in Table 2, are on the same order but generally less than $I_{sp,ideal}$. There is therefore a suggestion that TOF specific impulse may tend to underestimate true specific impulse. This idea is corroborated by previous studies that have shown TOF-inferred thrust tending to slightly overestimate direct thrust measurements [16,19,20], and an artificially high thrust estimate would correlate with an artificially low specific impulse estimate. Future work should aim to address the relevance of indirect specific impulse estimates through controlled comparison to direct measurements, similar to what has been done for direct and indirect thrust.

VI. Conclusion

Methods for improving thrust density in ionic liquid ion thrusters are necessary for ILITs to become more useful for a broad range of satellite classes. Here, we describe and characterize a design for an ILIT with highly densified emitter arrays with the aim of achieving much larger thrust levels than current state-of-the-art technology in the same physical footprint and without significant loss of performance. First, an emitter containing a single tip was characterized to establish the baseline performance of any individual tip in the larger and denser arrays. The single emitter data showed potential for excellent propulsive performance when extrapolated to a full array. In particular, beam angles were relatively small, energy spectra were typical for EMI-BF_4 ion beams and yielded high energy efficiencies, and mass spectra showed beams consisting of primarily pure ions, resulting in fast-moving particles and high values of specific impulse.

The data collected from a full thruster array consisting of 676 tips spaced 254 µm apart were comparable to that of the single emitter. The magnitude of the total array current compared to that of the single tip suggests the possibility that all or most of the tips in the array are activated and fire with a high degree of uniformity. In addition, the energy and mass spectra for the full array mirror well those for the single emitter, which is to be expected for a properly-functioning thruster. Angular beam distributions for the full thruster array were much wider than those for the single emitter, which is also to be expected because beams from an array superimpose hundreds of individual ion beams, each of which can have a central angle that is offset from the others, resulting in a full ion beam with a larger angular spread than any individual tip. This spread was also seen to increase with current, suggesting the possibility that multiple emission sites are present on at least some of the tips at the higher current setpoints.

All propulsive performance metrics measured for the thruster were estimated via indirect methods using

the beam diagnostics. While indirect estimates for metrics of interest such as thrust, specific impulse, and efficiency have been shown to be fairly reliable when compared to direct measurements, it is important to note that the indirect methods come with limitations. While no direct measurements were performed in this work, with the exception of total mass loss, future work will close this gap by performing direct measurements of important propulsive characteristics such as thrust and specific impulse.

Acknowledgments

Funding for this work was provided by a National Science Foundation Graduate Research Fellowship under grant 1745302. Paulo Lozano thanks the Miguel Alemán-Velasco Foundation for its support.

DISTRIBUTION STATEMENT A. Approved for public release. Distribution is unlimited.

This material is based upon work supported by the Department of the Air Force under Air Force Contract No. FA8702-15-D-0001. Any opinions, findings, conclusions or recommendations expressed in this material are those of the author(s) and do not necessarily reflect the views of the Department of the Air Force.

References

[1] Takao, Y., Inoue, N., Suzuki, K., Tachibana, F., Nagao, M., and Murakam, K., "Development of Ionic Liquid Electrospray Thrusters with a Massive Emitter Array for Higher Thrust Density," *36th International Electric Propulsion Conference*, Vienna, Austria, 2019, pp. IEPC–2019–149.

[2] Takao, Y., Suzuki, K., Guo, S., Nagao, M., Murakami, K., and Murata, H., "High-Current-Density Ionic Liquid Electrospray Thruster with a Nano-Capillary Emitter Array," *37th International Electric Propulsion Conference*, Cambridge, USA, 2022, pp. IEPC–2022–192.

[3] Shingu, T., Nagao, M., Murakami, K., Murata, H., Khumpuang, S., Hara, S., and Takao, Y., "Fabrication and Demonstration of SU-8 Based Emitter Arrays for Ionic Liquid Electrospray Thrusters," *Journal of Evolving Space Activities*, Vol. 1, 2023, p. 30. https://doi.org/10.57350/jesa.30.

[4] Villegas, D., Wijnen, M., Correyero, S., Arboleya, G., and Fajardo, P., "Impact of the propellant temperature on the performance of externally wetted electrospray thrusters," *37th International Electric Propulsion Conference*, Cambridge, USA, 2022, pp. IEPC–2022–212.

[5] Ramos, R., Correyero, S., Arboleya, G., Sepulveda, B., and Cruz, J., "Degradation mitigation strategies in electrospray thrusters based on chemically robust thin films," *37th International Electric Propulsion Conference*, Cambridge, USA, 2022, pp. IEPC–2022–220.

[6] de Borja De Saavedra, F., Wijnen, M., Correyero, S., Arboleya, G., and Perez, D., "Direct thrust measurements of an externally wetted electrospray thruster," *37th International Electric Propulsion Conference*, Cambridge, USA, 2022, pp. IEPC–2022–223.

[7] Siegel, N. W., "Silicon Wafer Integration of Ion Electrospray Thrusters," Master's thesis, Massachusetts Institute of Technology, Cambridge, MA, May 2020.

[8] Corrado, M. N., "Active Thermal Augmentation and Ultra Dense MEMS-Based Electrospray Thrusters," Master's thesis, Massachusetts Institute of Technology, Cambridge, MA, May 2022.

[9] Corrado, M. N., Lozano, P. C., Parameswaran, L., Cook, M., Holihan, E. C., Mathews, R., Racz, L. M., and Smith, M. A., "Densification of Ionic Liquid Electrospray Thrusters using Silicon-Based MEMS Fabrication," *37th International Electric Propulsion Conference*, Cambridge, USA, 2022, pp. IEPC–2022–177.

[10] Smith, M. A., Berry, S., Parameswaran, L., Holtsberg, C., Siegel, N., Lockwood, R., Chrisp, M. P., Freeman, D., and Rothschild, M., "Design, simulation, and fabrication of three-dimensional microsystem components using grayscale photolithography," *Journal of Micro/Nanolithography, MEMS, and MOEMS*, Vol. 18, No. 4, 2019, pp. 1 – 14. https://doi.org/10.1117/1.JMM.18.4.043507.

[11] Pettersson, G. M., Bruno, A. R., Corrado, M. N., and Lozano, P. C., "Performance Measurement and Propellant Testing for the STEP-1 CubeSat Electrospray Thrusters," *37th International Electric Propulsion Conference*, Cambridge, USA, 2022, pp. IEPC–2022–216.

[12] Freeman, D. S., "Design and Manufacture of the Next Generation of Ion Electrospray Thrusters," Master's thesis, Massachusetts Institute of Technology, Jun. 2019.

[13] MacArthur, J., Kristinsson, B. Ö., Freeman, D., Petro, E., Li, H., and Lozano, P. C., "Microfluidic and Extractor Electrode Update in the ion-Electrospray Propulsion System," *36th International Electric Propulsion Conference*, Vienna, Austria, 2019, pp. IEPC–2019–909.

[14] Kristinsson, B. Ö., Freeman, D., Petro, E., and Lozano, P. C., "Operation and Performance of a Fully-Integrated ionic-Electrospray Propulsion System," *36th International Electric Propulsion Conference*, Vienna, Austria, 2019, pp. IEPC–2019–646.

[15] Guerra-Garcia, C., Krejci, D., and Lozano, P., "Spatial uniformity of the current emitted by an array of passively fed electrospray porous emitters," *Journal of Physics D: Applied Physics*, Vol. 49, No. 11, 2016, p. 115503. https://doi.org/10.1088/0022-3727/49/11/115503.

[16] Corrado, M. N., Bruno, A. R., and Lozano, P. C., "Direct and Indirect Thrust Measurements of Ionic-Liquid Electrospray Thrusters on a Magnetically-Levitated Testbed," *AIAA SCITECH 2024 Forum*, 2024, pp. AIAA 2024–1344. https://doi.org/10.2514/6.2024-1344.

[17] Ziemer, J. K., "Performance of Electrospray Thrusters," *31st International Electric Propulsion Conference*, Ann Arbor, USA, 2009, pp. IEPC–2009–242.

[18] Petro, E., Bruno, A., Lozano, P., Perna, L. E., and Freeman, D., "Characterization of the TILE Electrospray Emitters," *AIAA Propulsion and Energy Forum*, Virtual Event, 2020, pp. AIAA 2020–3612. https://doi.org/10.2514/6.2020-3612.

[19] Courtney, D. G., Dandavino, S., and Shea, H., "Comparing Direct and Indirect Thrust Measurements from Passively Fed Ionic Electrospray Thrusters," *Journal of Propulsion and Power*, Vol. 32, No. 2, 2016, pp. 392–407. https://doi.org/10.2514/1.B35836.

[20] Krejci, D., Mier Hicks, F., Thomas, R., Haag, T., and Lozano, P. C., "Emission Characteristics of Passively Fed Electrospray Microthrusters with Propellant Reservoirs," *Journal of Spacecraft and Rockets*, Vol. 54, No. 2, 2017, pp. 447–458. https://doi.org/10.2514/1.A33531.